Supporting Information for

Molecular Dynamics Investigation of Surface Resistances in Zeolite Nanosheets

Omar Knio, Hanjun Fang, Salah Eddine Boulfelfel, Sankar Nair, David S. Sholl

School of Chemical & Biomolecular Engineering, Georgia Institute of Technology, 311 Ferst Drive NW, Atlanta, GA 30332-0100

CORRESPONDING AUTHOR: david.sholl@chbe.gatech.edu

Table of Contents

S.1　Hill Sauer Implementation

Boulfelfel et al. modified the Hill Sauer force field for a better description of zeolite pore dimensions.[1] They changed the equilibrium angle of the Si-O-Si and O-Si-O terms while keeping all other parameters constant.[1] The Hill-Sauer FF uses LAMMPS' Class 2 angle terms with the format

$$E = K_2(\theta - \theta_0)^2 + K_3(\theta - \theta_0)^3 + K_4(\theta - \theta_0)^4 + M(r_{ij} - r_1)(r_{jk} - r_2) +$$

$$N_1(r_{ij} - r_1)(\theta - \theta_0) + N_2(r_{jk} - r_2)(\theta - \theta_0) \qquad\qquad (S.1)$$

where i-j-k refer to the order of the three atoms, K, M, and N are energy scalars, θ_0 is the equilibrium angle, θ is the angle between the three atoms, r_1 and r_2 are the equilibrium bond distances between atoms i-j and j-k respectively, r_{ij} and r_{jk} are the bond distances between atoms i-j and j-k respectively.[2] Boulfelfel et al. only changed the θ_0 terms for both angles and kept all other distance and scalar terms at their original values.[1] The Boulfelfel et al. terms used in this study and the original terms are shown in **Table S.1** for comparison.

Table S.1 – Equilibrium Angle Comparisons

	Si-O-Si	O-Si-O
θ_0 – Original Hill-Sauer[3]	173.7651	112.0200
θ_0 – Boulfefel et al.[4]	150.0	113.0

There are other parameters in the Hill-Sauer force field that use the Si-O-Si and O-Si-O θ_0 such as dihedral and improper terms. However, Boulfelfel et al. kept the original Hill-Sauer θ_0 for the angle component of these terms, so we followed their example in our work as well.[3]

S.2　DFT-derived Force Field Parametrization for CO_2 and H_2

Fang et al. developed a first-principles-based force field for CO_2 in siliceous zeolites that showed good transferability across different zeolite topologies.[5] This approach

used the fully periodic framework to represent the adsorbent structure and relies on electronic structure calculations for hundreds or thousands of adsorption configurations randomly scattered throughout the framework. This approach was later extended to develop parameters for CH_4 in siliceous zeolites that can accurately predict both adsorption and diffusion properties.[6] In those studies, the charges for CH_4 and zeolite atoms were obtained from the density derived electrostatic and chemical (DDEC) method while the charges for CO_2 were obtained from the EPM2 model.[7-10] In this manuscript, we developed first-principles-based force fields for CO_2 and H_2 in bulk and nanosheet siliceous zeolites that use atomic charges from the Hill Sauer force field, since these charges are quite different than DDEC charges.[11, 12] We used the EPM2 model for $CO_2…CO_2$ interactions; this model correctly captures the phase behavior of pure CO_2.[10] $H_2…H_2$ interactions were treated as a three-point model used previously by Yang et al.[13]

S.2.1   Generating Training Sets for Force Field Fitting

The first step in force field fitting is the generation of a training set of atomic coordinates that adequately samples the potential energy surface. We generated one training set to describe adsorbate interactions with the bulk zeolite (Si, O_{SiOSi}) using biased molecular dynamics (MD) and another training set to describe adsorbate interactions with the hydrogen of silanol groups (H_{OH}) using Grand Canonical Monte Carlo (GCMC). The biased MD method is useful for deriving a force field that is accurate for both adsorption and diffusion properties because it generates adsorbate configurations in both pore and cage regions.[6]

We generated bulk zeolite adsorbate coordinates using half the cage volume of Zeolite A (LTA) as shown in **Figure S.1**. We divided this volume into six bins with equal width (1 Å) parallel to the 8-ring plane. In each bin we performed a biased NVT molecular dynamics (MD) simulation for 200 ps after an equilibration period of 100 ps. Each simulation had one adsorbate and used a

time step of 1 fs. Configurations were collected every 0.5 ps for a total of 2400 (400 from each bin). We used biased molecular dynamics to ensure that adsorbates remain inside their cage so that our configuration sample is representative. An unconstrained adsorbate will likely oversample the cage and undersample the transition state region. We confined each adsorbate near to its bin-defining plane with a harmonic spring constant of 15 kcal/mol using the COLVARS package[14] from LAMMPS[15]. In all biased MD simulations, the adsorbent atoms were fixed and only the adsorbate was allowed to move. The force field we used for the initial simulation was derived from Grimme's empirical dispersion expression in the DFT-D2 method,

$$C_6^{ij} = 4\varepsilon_{ij}\sigma_{ij}^6 \ \ and \ C_{12}^{ij} = \frac{\left(R_0^i + R_0^j\right)^6}{2}C_6^{ij} = 4\varepsilon_{ij}\sigma_{ij}^{12} \tag{S.2}$$

where R_0^i and R_0^j are the Van der Waals radii of each atom.[16] Grimme's work lists parameters for C_6 and R_0 for elements from H to Xe.[16] The C_6^{ij} term is defined as

$$C_6^{ij} = \sqrt{C_6^i C_6^j} \tag{S.3}$$

where the superscripts refer to the element described by C_6.[16] Solving equation S.2 gives ε_{ij} and σ_{ij}. The ε_{ij} and σ_{ij} terms are used to calculate the van der Waals energy in our MD simulations using the 12-6 form of the Lennard-Jones equation

$$E_{vdW} = E_{Lennard-Jones} = 4\varepsilon_{ij}\left[\left(\frac{\sigma_{ij}}{r}\right)^{12} - \left(\frac{\sigma_{ij}}{r}\right)^6\right] \tag{S.4}$$

where r is the distance between both atoms.
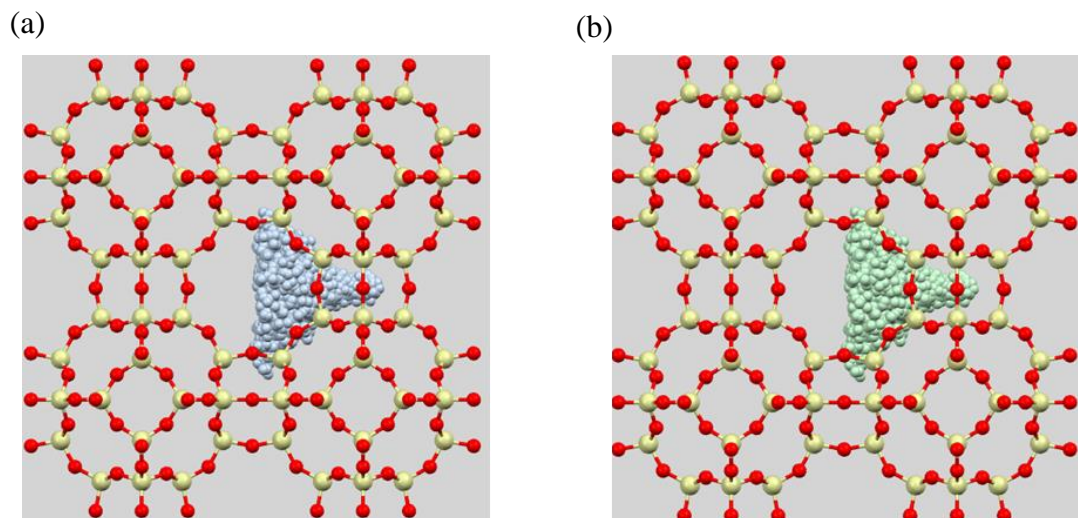
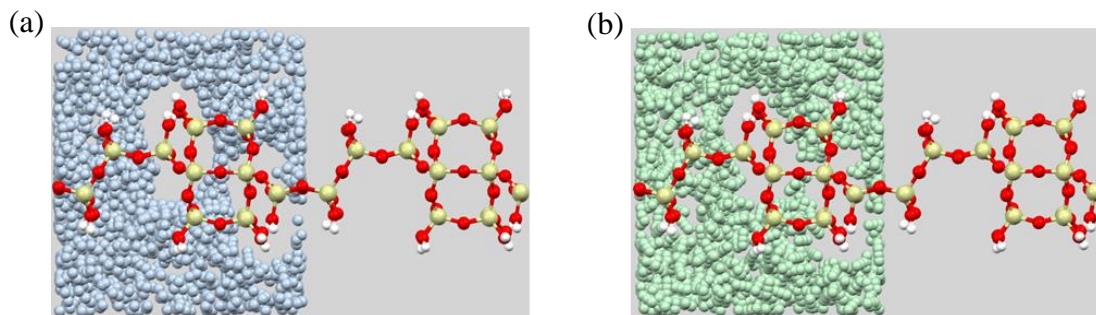**Figure S.1.** Illustration of the training sets used to fit force field parameters for (a) CO_2–framework and (b) H_2–framework interactions based on a bulk siliceous zeolite, Si-LTA. O, Si, CO_2 and, H_2 atoms are depicted as red, beige, blue and green respectively.

To make training sets for CO_2 and H_2 interactions with the hydrogen of the surface hydroxyl group (H_{OH}) on zeolite surfaces, we generated initial configurations using NVT Monte Carlo (N = 1, T = 300 K) on 9 Å CHA (101) nanosheets. We used the force field parameters derived from the bulk zeolites to define interactions with the Si, O_{SiOSi}, and O_{SiOH} atoms. The van der Waals (vdW) parameters for the oxygen atom of the hydroxyl group were assumed to be equivalent to those for framework oxygen atoms. The initial H_{OH} parameters were obtained from Grimme's empirical dispersion expression in the DFT-D2 method.[16] Based on the simulation snapshots, 800 configurations were randomly chosen as shown in **Figure S.2**.

Figure S.2: Illustration of the training sets used to fit force field parameters for (a) CO_2–hydroxyl and (b) H_2–hydroxyl interactions based on a two-dimensional chabazite nanosheet. O, Si, H, CO_2 and, H_2 atoms are depicted as red, beige, white, blue and green respectively.

S.2.2 *Adsorbate Zeolite Interactions*

After the training sets above were generated, our next step was to compute PBE DFT adsorbate–adsorbent interaction energies defined as:

$$E_{interaction}^{DFT} = E_{adsorbate,zeolite} - (E_{adsorbate} - E_{zeolite}) \qquad (S.5)$$

For each configuration, the total energy of the system (adsorbate + adsorbent) was calculated, then the energies of the empty adsorbent and isolated adsorbate were subtracted to obtain the corresponding interaction energy. All DFT single-point calculations were performed using VASP package[17-20] version 5.4.4 in combination with projector augmented wave (PAW) pseudopotentials.[21, 22] A plane-wave basis set energy cut-off equal to 520 eV was used. Gaussian electronic smearing with width equal to 0.2 eV was applied. A Blocked Davidson electronic minimization algorithm was used to calculate the electronic ground state, with convergence stopping criterion set to 10^{-4} eV. It has been shown that dispersion corrections are important for accurately describing interactions between adsorbate molecules and zeolites, and the DFT/CC (density functional theory/coupled cluster) method performs well for these system,[5, 23] so the CC corrections that were developed previously for adsorption of CO_2 and H_2 in zeolites were added to the PBE interaction energies.[24, 25]

The electrostatic part of the interaction energy was independently computed for each configuration using Ewald summation. After computing $E_{interaction}^{DFT/CC}$ and $E_{Coulomb}^{FF}$, the fitting itself involved least-squares regression to determine new values for C_6^{ij} and C_{12}^{ij} in equation S.6.

$$E_{vdW}(R_{ij}) = E_{Lennard-Jones}(R_{ij}) = \frac{C_{12}^{ij}}{R_{ij}^{12}} - \frac{C_6^{ij}}{R_{ij}^6} \qquad (S.6)$$

To calculate bulk parameters, we fitted equation S.6 to 2400 configurations then used the bulk parameters in the next iteration of the biased NVT MD simulations. This procedure was performed for 3-6 iterations until the fitted force field parameters were converged (the changes of parameters are within ±3%). For nanosheets, we were unable to obtain complete convergence of the potential parameters (i.e. all parameter value's Δ < 3%) after six iterations, so we chose to use the configurations from last three iterations to finalize force field parameters. The resulting force field (denoted CCFF) parameters for CO_2 and H_2 in bulk siliceous zeolites and zeolite nanosheets are summarized in **Table S.2**.

Table S.2: CO_2 and H_2 Self Interaction and Zeolite Interaction Parameters

Self Interaction	Reference	ϵ/k_B (K)	σ (Å)	Charge (e)
C_CO2	[10]	28.129	2.757	0.6512
O_CO2	[10]	80.507	3.033	-0.3256
H_H2	[26]	NA	NA	0.468
c_H2	[26]	36.7	2.96	-0.936
C=O bond 1.149 (Å) [10]		H-H bond 0.74 (Å) [26]		
Hill-Sauer Charge				
Si	[3]			0.5236
Oz (O_SiOSi)	[3]			-0.2618
Oz (O_SiOH)	[3]			-0.195
H (H_OH)	[3]			0.0641
CO_2 Cross Species				
C_CO2 – Oz	This work	28.610	3.016	
O_CO2 – Oz	This work	35.549	3.140	
C_CO2 – Si	This work	60.747	3.560	
O_CO2 – Si	This work	47.494	3.436	
C_CO2 – Hz	This work	50.515	2.424	
O_CO2 – Hz	This work	42.073	2.316	
H_2 Cross Species				
c_H2 – Oz	This work	31.726	2.971	
c_H2 – Si	This work	47.376	3.446	
c_H2 – Hz	This work	19.213	2.348	
H_H2 – All atoms		NA	NA	

S.2.3 Force Field Analysis

In the FF fitting, the residual standard deviation (RSD) is minimized,

$$RSD = \sqrt{\frac{\Sigma_k^n\left(E_{FF}^k - E_{DFT/CC}^k\right)^2}{n-2}} \tag{S.7}$$

where E_{FF}^k is the interaction energy calculated at the FF level for configuration k, $E_{DFT/CC}^k$ is the

interaction energy calculated at the DFT/CC level, and n is the number of configurations for our

FF fitting dataset. The mean deviation (MD) is also calculated after the parameterization,

$$MD = \frac{\sum_k^n \left(E_{FF}^k - E_{DFT/CC}^k\right)}{n} \tag{S.8}$$

The RSD and MD can give an overall evaluation of the performance of the fitted FF in reproducing the ab initio data.
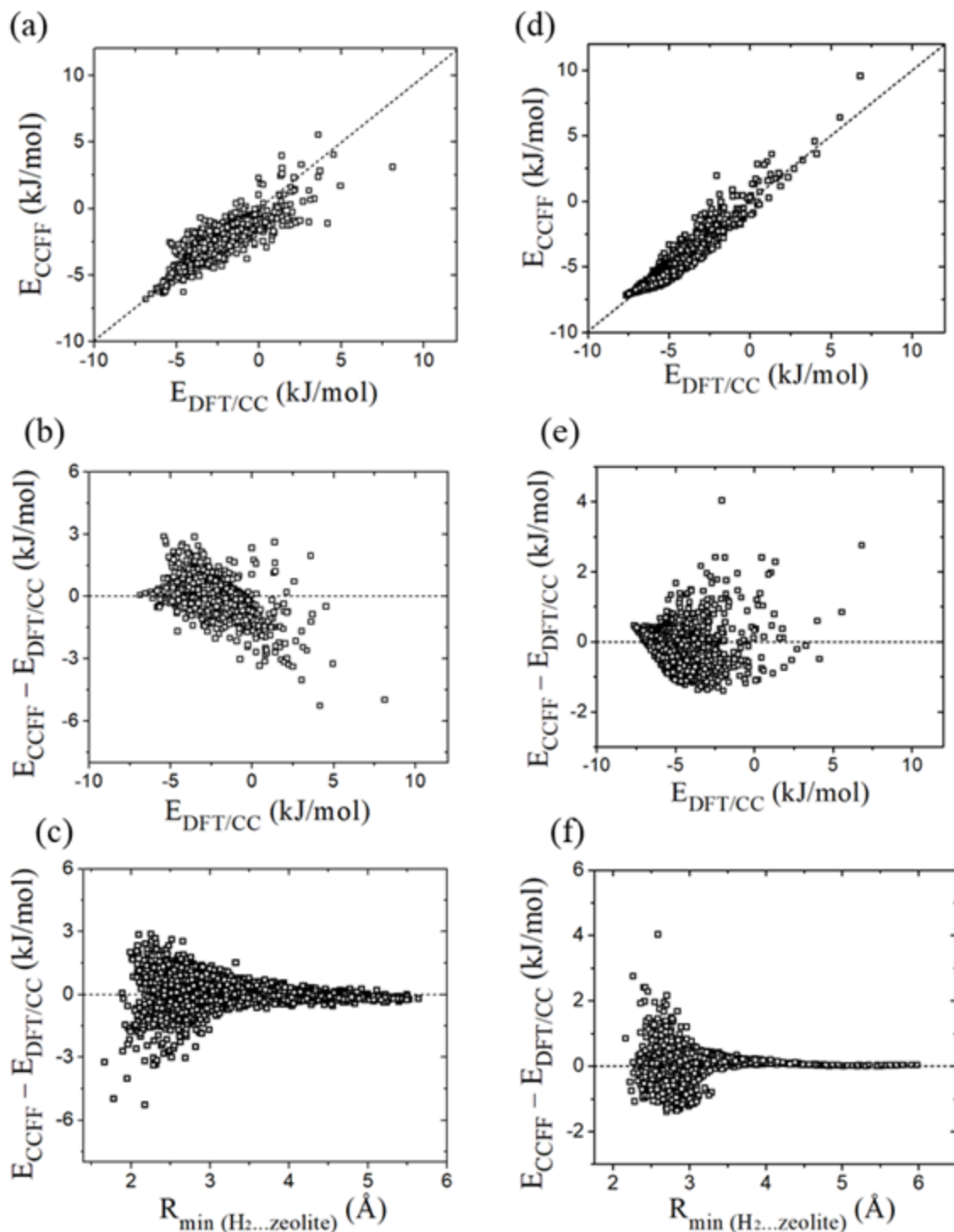
A comparison of the interaction energies predicted with CCFF and the corresponding energies at the DFT/CC level for CO_2 and H_2 in bulk Si-LTA and nanosheet CHA is shown in **Figures S.3** and **S.4**. For CO_2 in Si-LTA, the DFT/CC calculations of the last iteration span a range of adsorption energies, from -31 to 2 kJ/mol. The CCFF underestimates the most energetically favorable configurations by about 8 kJ/mol, and overestimates the least stable configurations by 11 kJ/mol. This imperfect fit is also observed as high RSD and MD values of 2.8 and -0.3 kJ/mol, respectively. A similar trend is seen with CO_2 in nanosheet CHA.

For H_2 in Si-LTA and OH-CHA-2D, the fitting results are better than those from CO_2. The CCFF reproduces the DFT/CC interaction energies for both energetically favorable and unfavorable configurations, with and RSD and MD 0.4 and 0.04 kJ/mol for H_2 in Si-LTA, and 0.7 and 0.02 kJ/mol for H_2 in OH-CHA-2D.

In Fang et al.'s previous work, we obtained a better fit for CO_2 interactions with Si-CHA where the fitted force field describes both favorable and unfavorable configurations reasonably well.[5, 23] This is probably due to the smaller charges of the Hill-Sauer force field, which has weaker Coulomb interactions that cannot be fully compensated by vdW interactions via force field fitting.
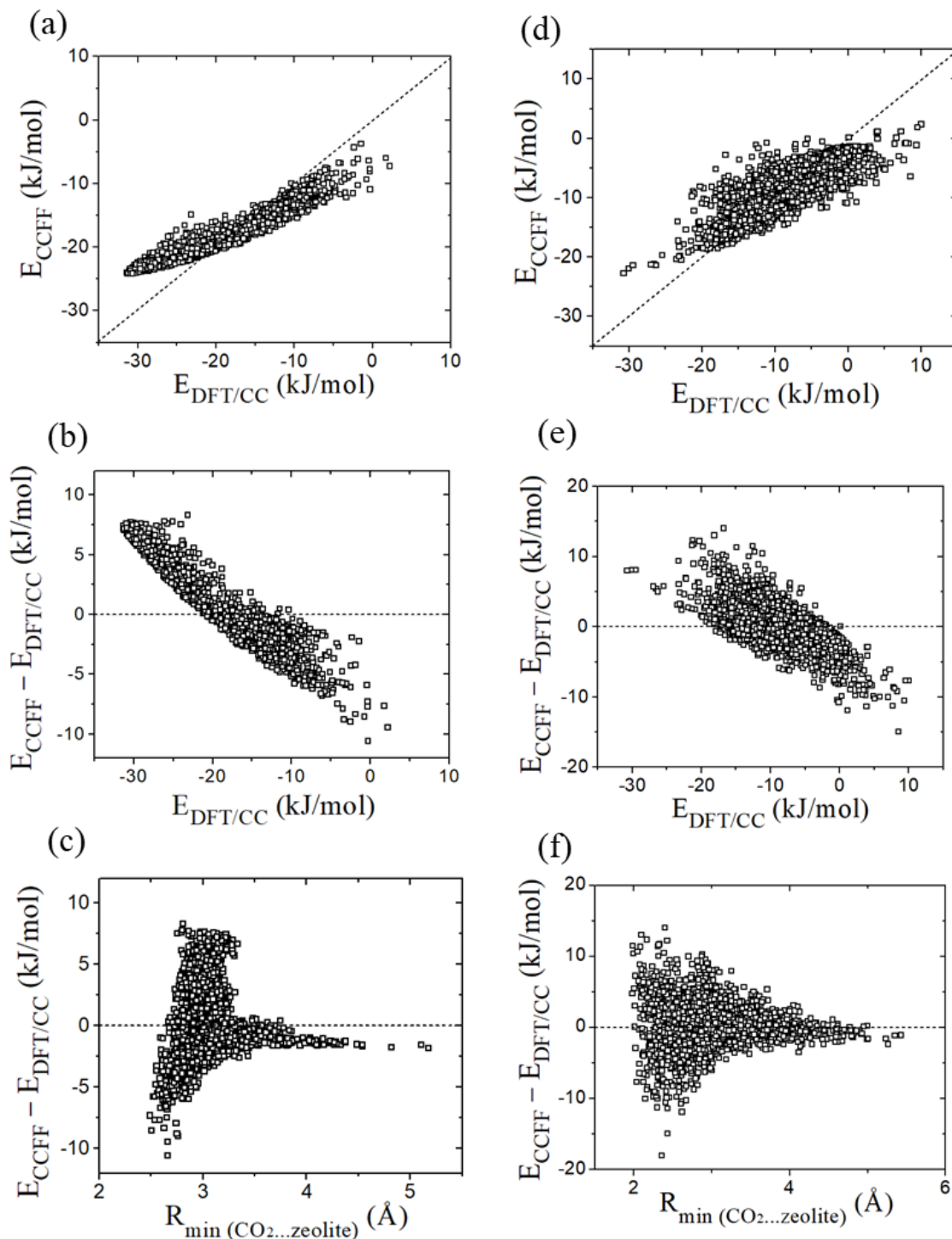
Figure S.3: Force field fitting results for CO_2 in (a–c) Si-LTA and (d–f) OH-CHA-2D: (a, d) Comparison of the interaction energies of CO_2 in zeolite for CCFF and DFT/CC, (b, e) the difference in interaction energies ($E_{CCFF} - E_{DFT/CC}$) as a function $E_{DFT/CC}$, and (c, f) $E_{CCFF} - E_{DFT/CC}$ as a function of the nearest interatomic distance between the atoms of CO_2 and zeolite. A total of 2400 CO_2 configurations are included for both bulk Si-LTA and nanosheet Si-CHA.

Figure S.4: Force field fitting results for H_2 in (a–c) Si-LTA and (d–f) OH-CHA-2D: (a, d) Comparison of the interaction energies of H_2 in zeolite for CCFF and DFT/CC, (b, e) the difference in interaction energies ($E_{CCFF} - E_{DFT/CC}$) as a function $E_{DFT/CC}$, and (c, f) $E_{CCFF} - E_{DFT/CC}$ as a function of the nearest interatomic distance between the atoms of H_2 and zeolite. A total of 2400 H_2 configurations are included for both bulk Si-LTA and nanosheet Si-CHA.

We validated the CCFF listed above by comparing the simulated adsorption isotherms and heats of adsorption for CO_2 in siliceous chabazite (Si-CHA) with available experimental data. The validation results are shown in **Figures S.5**. CCFF predicts adsorption isotherms well for CO_2 in Si-CHA at 301 and 323 K compared to experimental data from Fang et al. and Pham et al.[5, 27] The heats of adsorption predicted using CCFF agree reasonably well with the calorimetric data from Fang et al.[5] and the results from Pham et al. that were obtained from the isotherm data using the Clausius-Clapeyron equation.[27] The deviation is about 2–3 kJ/mol at all loadings. We note that it is not possible to validate our FF against equilibrium adsorption data for zeolitic nanosheets because no experimental data of this kind is available.
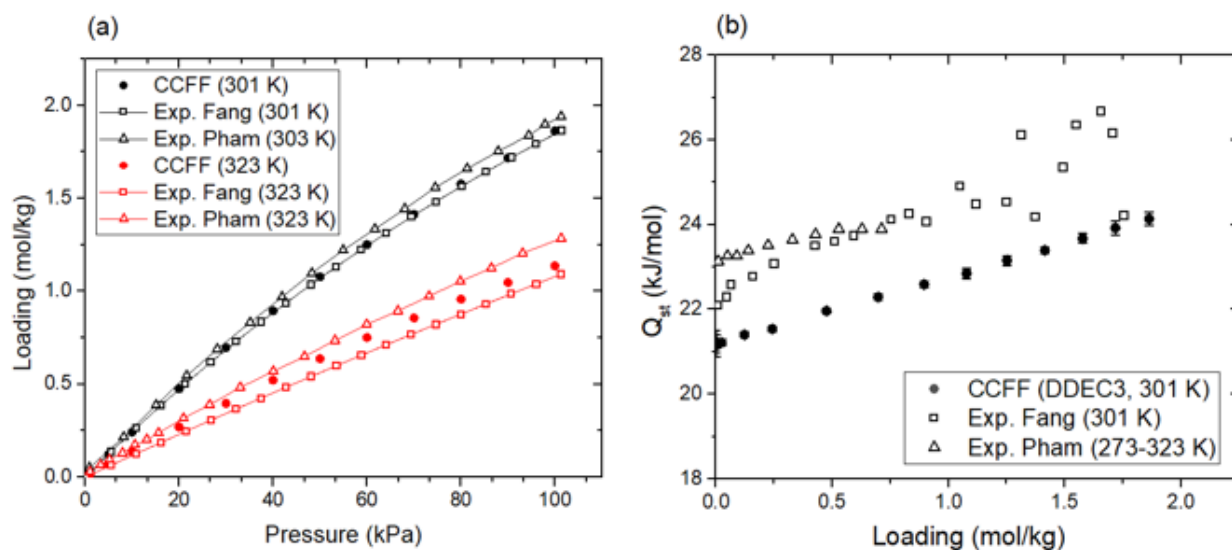
Figure S.5: Comparison of simulated and experimental (a) adsorption isotherms and (b) isosteric heats of adsorption for CO_2 in bulk Si-CHA. The experimental data are from Fang et al. and Pham et al.[5, 27]

S.3   Hydrocarbon Lennard-Jones Parameters

The hydrocarbon Lennard-Jones parameters for ethane, ethene, propane, and propene obtained from the TraPPE force field, and the zeolite Lennard-Jones parameters obtained from the TraPPE-zeo force field are listed in **Table S.3**.[28-30]

Table S.3 – Hydrocarbon Lennard-Jones Parameters

Self Interaction	Reference	ϵ/k_B (K)	σ (Å)	Charge (e)
CH_{3_sp3}	29	98.0	3.75	0
CH_{2_sp3}	29	46.0	3.95	0
CH_{2_sp2}	30	85.0	3.675	0
$CH_{\_sp2}$	30	47.0	3.73	0
Si	28, 31	22	2.3	0.5236
Oz (O_{SiOSi})	28, 31	53	3.3	-0.2618
Oz (O_{SiOH})	31	53	3.3	-0.195
Hz	31	NA	NA	0.0641

We simulated hydrocarbons as flexible molecules using the parameters given by Granato et al.[32] The parameters in **Table S.4** refer to the following bond and angle potentials

$$u_{bond} = \frac{k_1}{2}(r - r_0) \qquad u_{angle} = \frac{k_2}{2}(\cos\theta - \cos\theta_0) \qquad (S.9)$$

where u_{bond} is the bond energy, k_1 is an energy scalar, r is the distance between both atoms, r_0 is the equilibrium bond distance, u_{angle} is the angle bending energy, k_2 is an energy scalar, θ is the angle formed by three atoms, and θ_0 is the equilibrium angle.

Table S.4 – Hydrocarbon Flexibility Parameters[32]

	Single Bond		Double Bond		Angle	
	r_0 (Å)	k_1/k_B (K/Å^2)	r_0 (Å)	k_1/k_B (K/Å^2)	θ_0 (°)	k_2/k_B (K)
Ethane	1.54	96,500	NA	NA	NA	NA
Ethene	NA	NA	1.33	96,500	NA	NA
Propane	1.54	96,500	NA	NA	114	62,500
Propene	1.54	96,500	1.33	96,500	119.7	70,400

The CH_4 self-interaction parameters from the TraPPE force field and the CH_4 zeolite interactions from the work of Fang et al. are listed in **Table S.5**.[29, 33]

Table S.5 – CH$_4$ Lennard-Jones Parameters

Self-Interaction	Reference	ϵ/k_B (K)	σ (Å)	Charge (e)
CH_4	[29]	147.9	3.73	0
CH$_4$ Cross Species				
CH_4 – Oz	[33]	109.156	3.3815	
CH_4 – Si	[33]	0	0	
CH_4 – Hz		NA	NA	

S.4 Slab Thermalization

Several NEMD studies have shown that it is critical to model the adsorption and desorption step in simulations of porous nanosheets accurately. Newsome and Sholl showed that a rigid zeolite framework increases surface resistance by repelling attempts at adsorption.[34] Liu, Nicholson, and Bhatia showed that a temperature gradient develops due to the exothermic/endothermic heats of adsorption/desorption at opposite ends of the nanotube.[35] As a result of the temperature gradient, their NEMD simulations resulted in slightly higher flux compared to the EMD case.[35]

In our simulations, we wanted to allow for local cooling and heating upon desorption and adsorption, so we modeled the edges of our zeolite nanosheets using an NVE thermostat. The interior of the nanosheet was modeled using an NVT thermostat to prevent energy drift. **Figure S.6** shows an example of a 14 nm MFI (010) nanosheet with a 4 nm NVT thermostat in the interior and a 5 nm NVE thermostat at each end.
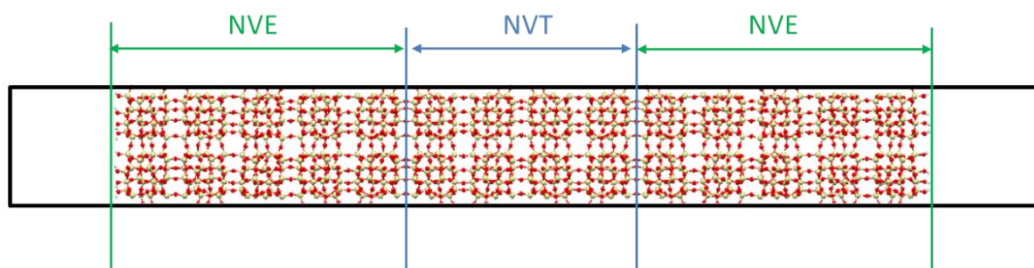
Figure S.6. An MFI (010) 14 nm slab with a 4 nm NVT thermostat in the center and an NVE thermostat at each end.

We conducted several simulations to find an appropriate thickness of the NVT region. Ideally the region should be thick enough to maintain constant temperature, but no thicker, lest the thermostat interfere with adsorption and desorption kinetics. For each simulation, any zeolite atom not in the NVT region was included in the NVE regions. We ran EMD simulations of CO_2 in a 14 nm MFI (010) slab at 2 bar and 300 K with a 1 fs time step for 1 ns. Our data was saved every 100 ps and we averaged over 15 independent simulations. To measure desorption, we counted the number of molecules that crossed the cell boundary. We defined a desorption constant equal to

$$k_{des} = \frac{j}{AC} \tag{S.10}$$

where j is the flux out of the slab, A is the surface area of the slab, and C is the concentration of adsorbate in the slab.[36]

Figure S.7(a) shows the effect of the NVT region thickness on k_{des}, which increases from 0.2 to 0.5 nm, remains roughly constant from 0.5 to 8 nm, and increases thereafter. The initial increase can be explained by **Figure S.7(b)** which shows that a 0.2 nm NVT thermostat region is unable to maintain constant temperature. The increase in k_{des} from 8 nm onwards is due to the NVT thermostat's interference with the desorption process, where it likely replenishes the kinetic energy at the surface faster than it would be replenished via heat flux. We found that 0.5 nm was the thinnest NVT region that maintained a constant temperature, so a 0.5 nm NVT region was used in all slab simulations. We chose the thinnest region possible to ensure the ability to effectively simulate very thin slabs.
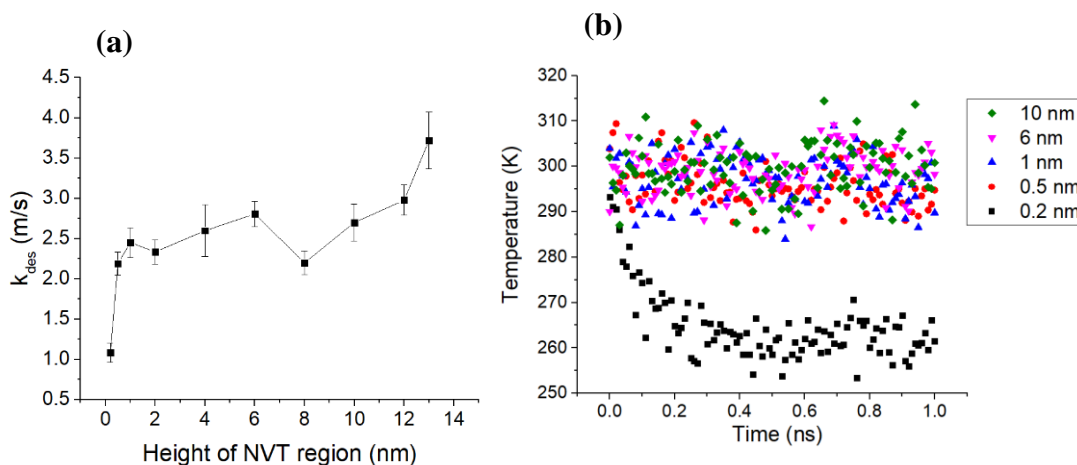
Figure S.7. Simulations of CO_2 in a 14 nm MFI slab at 2 bar and 300 K. (a) k_{des} increases with the thickness of the NVT region. (b) The system temperature holds steady for NVT regions at least 0.5 nm thick, but not for the 0.2 nm region. The legend lists the thickness of each NVT region tested.

S.5 Convergence

To calculate accurate diffusivities, it is standard practice to simulate a trajectory that is long enough to capture the characteristic diffusion length, the distance from one transition state to another. In LTA, for example, this is defined as the distance between the centers of two neighboring cages (1.2 nm).[33] Therefore, an LTA diffusion run that results in mean squared displacement (MSD) larger than 1.44 nm^2 implies than on average each molecule has hopped to a neighboring cage and overcome the energy barrier to diffusion at least once.

In slab unit cells, we assume that diffusion is encumbered by resistance inside the zeolite as well as desorption from the surface. Therefore, we defined the characteristic diffusion length as the total length of the unit cell as that would entail movement from the center of one slab to the center of its nearest image. **Figure S.8(a)** displays an MSD plot averaged over 20 runs of ethene diffusion through a 2 nm MFI (010) unit cell at 250 K and 1 molec/uc. Since the squared length of the unit cell is 36 nm^2, and the MSD at 50 ns is 1,648 nm^2, each adsorbate on average jumped to a neighboring slab 45 times.

Although we use the MSD to tell if a run was sufficiently long, we use the center of mass squared displacement (CoM SD) to obtain a diffusivity. The CoM SD for the ethene diffusion simulations is shown in **Figure S.8(b)**. The plot is not entirely linear, so a diffusivity derived from the slope will have a high standard deviation. Therefore, we break up the trajectories into non-overlapping time blocks, calculate the diffusivity using the slope of each block, and measure the standard error in the mean of the set of diffusivity values.[37] The average diffusivities and errors for the data in **Figure S.8** is shown in **Table S.6**, which shows that the error decreases as the time block size decreases.
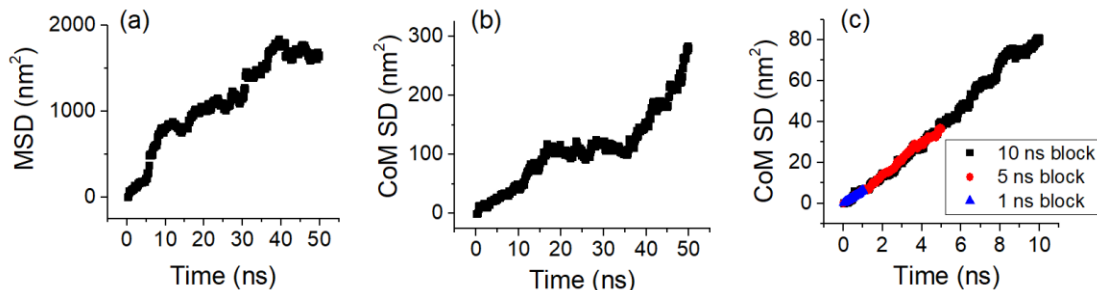
Figure S.8. Trajectories for diffusion of ethene through 2 nm MFI at 250 K and 1 molec/uc displaying (a) the MSD of the total run, (b) the CoM SD for the total run, and (c) the CoM SD for time blocks of different size.

Table S.6 – Diffusivity and Standard Error of Mean for Ethene in a 2nm MFI Slab

Time block (ns)	50	10	5	1
$D_{z,zeo}$ (m^2/s E-10)	2.5	3.9	3.7	3.7
s_m (m^2/s E-10)	1.8	1.1	0.9	0.7

In order to use the diffusivity from the 1 ns time block, it is best to ensure that it is statistically equivalent to output from larger time blocks. **Table S.6** shows that the diffusivity of the 1 ns time block is within the margin of error of the larger time blocks.[37] In addition, **Figure S.8(c)** shows that the slopes for various time blocks are overlapping. This data allows us to conclude that the 1 ns time block is sampling the same phenomena as larger time blocks.

There are some scenarios in which the diffusion mechanism observed at 1 ns is different than that observed at larger time intervals. **Figure S.9** shows trajectories for propane diffusion through a 10 nm MFI (010) slab at 250 K and 1 molec/uc. The CoM SD of different time blocks in **Figure S.9(c)** do not share the same slope. In this instance the 1 ns time block is capturing only diffusion through the slab, whereas the 5 ns and 10 ns time blocks capture both diffusion through the slab and desorption onto a neighboring slab. In such scenarios, we used the long time slope from the full 50 ns trajectory.
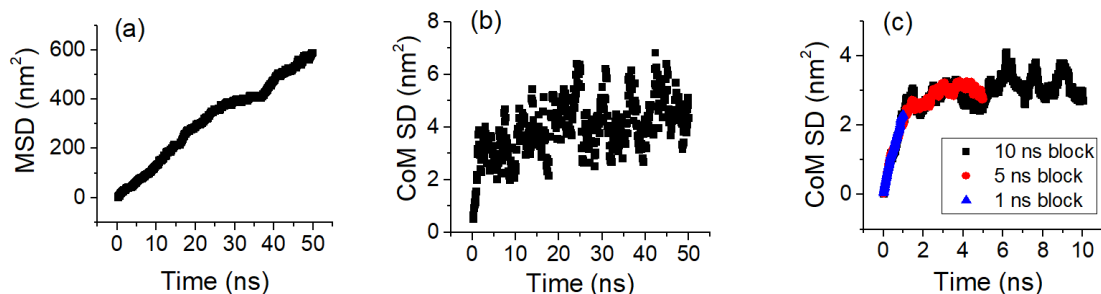
Figure S.9. Trajectories for diffusion of propane through 10 nm MFI at 250 K and 1 molec/uc displaying (a) the MSD of the total run, (b) the CoM SD for the total run, and (c) the CoM SD for time blocks of different size.

S.6   Defining the Zeolite/Gas Interface

In the main text of this manuscript, we describe using equation 4 to calculate an effective corrected diffusivity ($D_{z,zeo}$) across the zeolite nanosheet. Here, we describe how we define the boundary between the nanosheet and the gas layer. The adsorption profile for CO_2 in MFI at high loading in **Figure S.10(a)** shows that molecules form adsorption layers at both ends of the nanosheet. This external layering does not occur in all cases, as seen in the case of propane at low temperature and low loading in **Figure S.10(b)**.
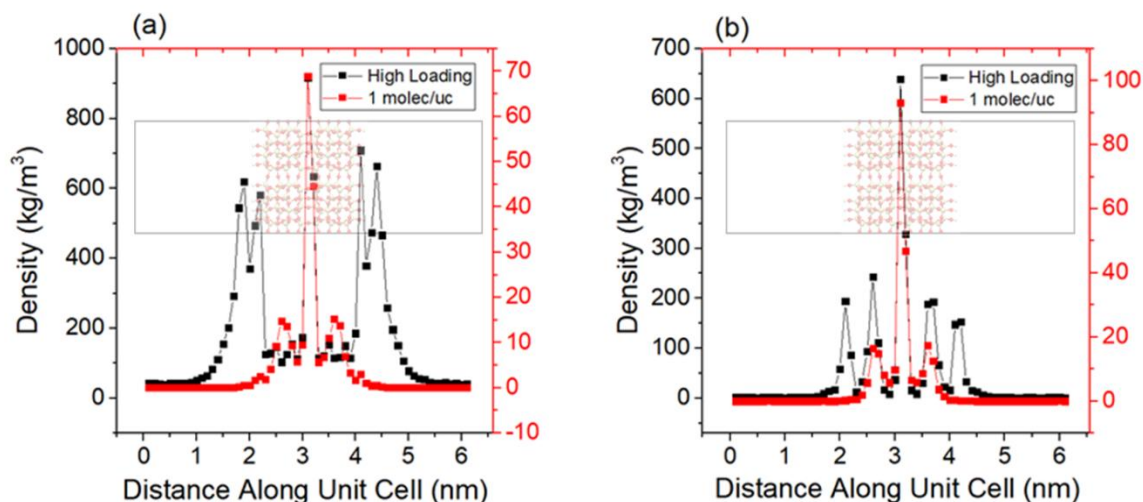
Figure S.10. Density profiles in a 2.2 nm MFI (010) slab at 250 K for (a) CO_2 and (b) propane. The unit cell is superimposed near the center of each graph.

To test whether the $D_{z,zeo}$ should be measured across a region that includes these adsorption layers, we calculated $D_{z,zeo}$ for CO_2 diffusion through a 2 nm MFI (010) unit cell using four different adsorption layer correction (L_{cor}) estimates. This correction was applied (shown in red) to equation 4 of the main text such that

$$D_{z,zeo} = \frac{N_{sys}^2}{2N_{zeo+cor}\left(\frac{L_{gas}-L_{cor}}{L_{zeo}+L_{Lcor}}+1\right)} \lim_{t\to\infty} \frac{1}{t} \langle \left|\Delta z_{sys,com}\right|^2 \rangle \tag{4}$$

$N_{zeo+cor}$ is the sum of the molecules of gas in the zeolite proper (silanol H on one end to silanol H on the opposite end) and the molecules inside the adsorption layers of length L_{cor} at each end.

Dutta and Bhatia tested two different values of L_{cor} (0 nm and total gas phase length) to distinguish internal and external resistance.[38] The equations they used to calculate diffusivity tracked a molecule's trajectory through a predetermined section of the nanosheet unit cell, as determined by L_{cor}.[38] If the section ended at the surface of the zeolite, the resistance the molecule encountered was due to the zeolite media and desorption. If the section encompassed the entire unit cell, then the molecule also encountered resistance from adsorption and gas phase movement.[38] Since our method to calculate surface resistance is functionally equivalent to theirs,[35, 38] we used different values of L_{cor} to quantify the magnitude of different resistances.

Our objective was to calculate the surface resistance due to adsorption and desorption. Since these events take place within the adsorption layers, the most accurate L_{cor} is one which captures the length of the adsorption layer(s) but no more. **Figure S.11** shows the surface resistances obtained for CO_2 diffusion through a 2 nm MFI unit cell using various L_{cor}. The "Tailored Manually" L_{cor} was obtained by visually estimating the size of the adsorption layer from adsorption profiles for each temperature and pressure condition and are listed in **Table S.7**. We

view this result as the correct value of L_{cor}, but it is impractical to estimate the value by hand for each simulation. Our aim below, therefore, is to establish an algorithmic approach to this issue.
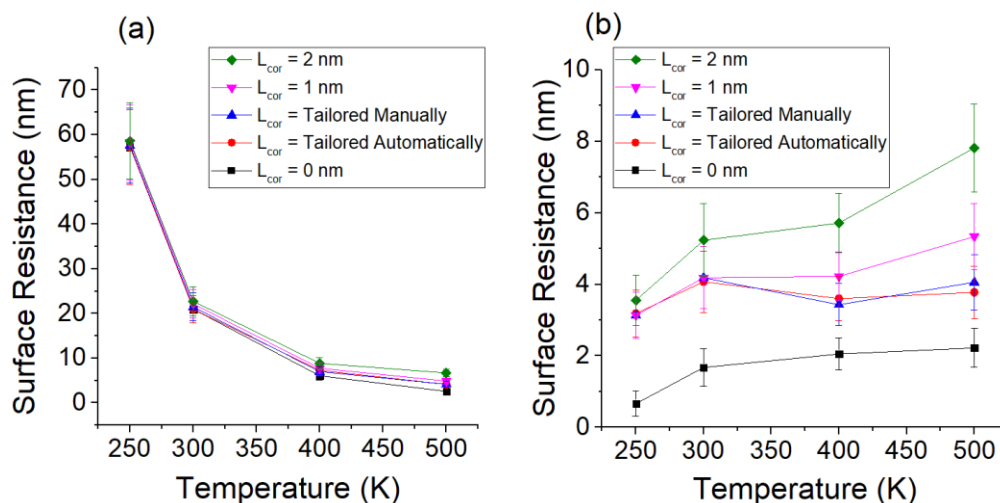
Figure S.11. A comparison of CO_2 surface resistance calculated using $D_{0,eff}$ measured across the length of the zeolite (without correction) or length of the zeolite and the adsorption layer (with correction) simulated at a loading of (a) 1 molec/uc and (b) high loading.

Table S.7 – Tailored L_{cor} for CO_2 in a 2 nm MFI Slab

Temperature	250 K	300 K	400 K	500 K
1 molec/uc L_{cor} (nm)	0.1	0.2	0.4	0.6
High Loading L_{cor} (nm)	1	1	0.5	0.5

Since the largest adsorption layers were ~1 nm in length, we first employed an L_{cor} of length 1 nm. We also tested L_{cor} with lengths 0 nm and 2 nm. **Figure S.11** shows that the L_{cor} value does not have a great effect on surface resistance when temperature and pressure are low, but it does have a greater effect when temperature and pressure are high. At high temperature and pressure, molecules spend a larger portion of time outside the nanosheet than they do at lower temperature and pressure, so larger L_{cor} measure larger gas phase resistances. Dutta and Bhatia found that gas phase resistance (adsorption and gas movement) only amounted to a maximum of

25% of total resistance.[38] We examined a wider range of conditions and found that adsorption and gas phase resistance can account for up to 70% of the total surface resistance.

Motivated by the results above we developed a simple algorithm to automatically determine L_{cor}. With this approach L_{cor} is defined to be the largest distance from the nanosheet surface at which the average density of the adsorbate is 10% larger than the average gas phase density. Comparisons between the automatically tailored approach and the manually tailored approach in **Figure S.11** show similar results, so we used this algorithm in all calculations reported in the manuscript.

S.7   Adsorbate Density in Nanosheets

Figure S.12 shows the propane density in an MFI (010) slab and an MFI (010) bulk structure. The average density in the bulk is 152 kg/m^3 while the average density in the slab is 118 kg/m^3, so the slab has 77% of the bulk density. The density profile in the bulk shows a repeat pattern of a large peak followed by two smaller peaks, with the large peaks occurring at the center of the MFI a and b channel intersections. The center of the MFI slab has such a channel intersection with an accompanying large peak. Though the surface on each side has half the volume of the full intersection, it has less than half of the full intersection density.
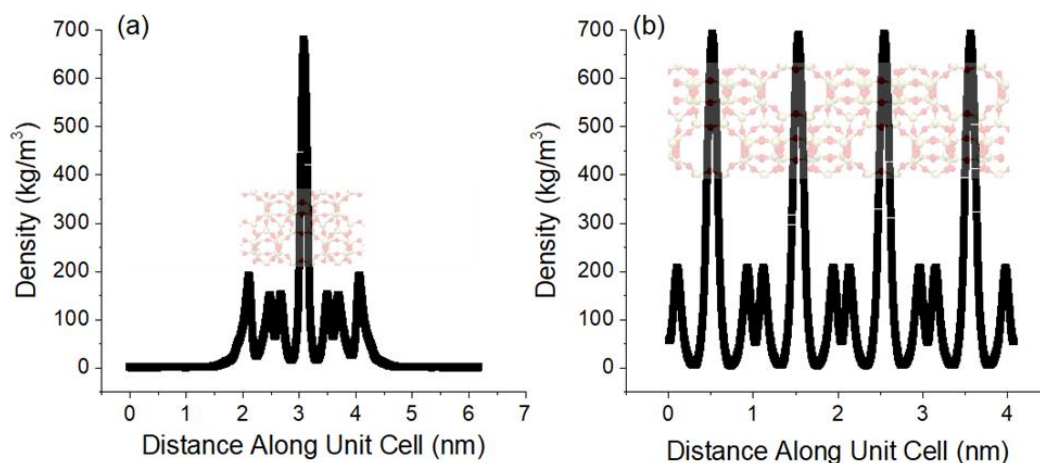
Figure S.12. The density profile of propane post equilibration at 0.5 bar and 250 K in an MFI (010) (a) 2 nm slab and (b) 4 nm bulk unit cell.

Figure S.13 shows the CO_2 density in an MFI (010) slab and an MFI (010) bulk structure. The average density in the bulk is 277 kg/m^3 while the average density in the slab is 269 kg/m^3, so the slab has 97% of the bulk density.
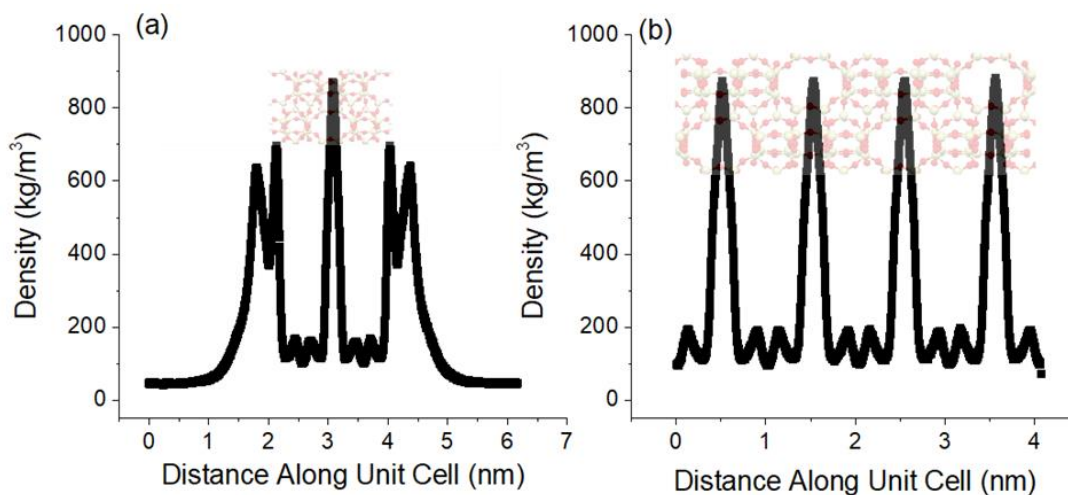
Figure S.13. The density profile of CO_2 post equilibration at 15 bar and 250 K in an MFI (010) (a) 2 nm slab and (b) 4 nm bulk unit cell.

S.8   Activation Energy

Figure S.14 shows an Arrhenius plot used to find the effective activation energies associated with the surface resistance in an MFI (010) nanosheet for the seven molecules we

studied. For this analysis we set R_{surf} equal to the surface resistance as defined in equation 6 rather than the surface resistance equivalent height as defined in equation 10 (and used in throughout the manuscript) to avoid including information from $D_{0,bulk}$ included in the latter term. Although some curvature can be seen in the data for propane and propene, the effective activation energies were obtained simply by linear fits to each data set in **Figure S.14(a)**.
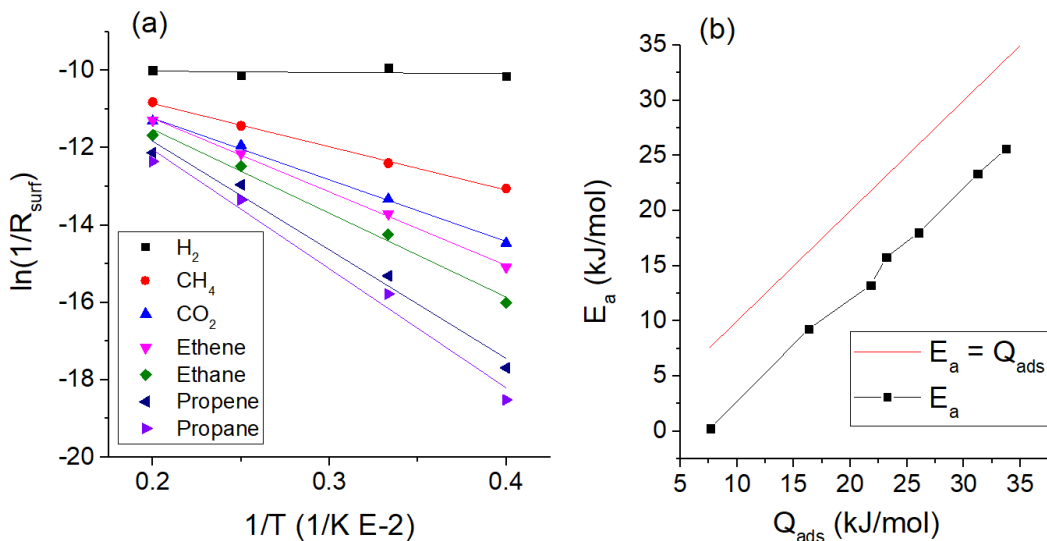
Figure S.14. (a) Arrhenius plots and lines of best fit based on the surface resistance in 2 nm MFI (010) slabs at a loading of 1 molec/uc. (b) The E_a graphed against the Q_{ads} for all seven molecules.

S.9   High Loading

The MFI surface resistances displayed in **Figure 2** of the main text were calculated at a high and low loading scenario. For low loading, we used one molecule in the slab unit cell, and two molecules in the MFI $1\times2\times1$ supercell. For high loading, we used the loadings shown in **Table S.8**. Some of the loadings in the bulk unit cell portion of the table have a ½ molecule because the GCMC simulation sometimes populates the $1\times2\times1$ supercell with an odd number of molecules but the numbers in **Table S.8** were divided in half to correspond to one unit cell. The slab is equivalent to one unit cell of MFI so the simulation loadings are reported as is.

Table S.8 – High Loading at each Temperature

Temperature (K)	Slab MFI (010) Loading (molec/uc)						
	H_2	CH_4	CO_2	ethane	ethene	propane	propene
250	28	31	47	19	18	11	11
300	22	22	36	25	23	12	12
400	15	12	18	17	17	21	20
500	12	8	11	11	10	12	12
	Bulk MFI (010) loading (molec/uc)						
250	10	16.5	22	16	16	12	12
300	6.5	13	19	15	15	11.5	11.5
400	3.5	6.5	12	11	10.5	10.5	10.5
500	2	3	6	5.5	6	7	7.5

To determine the saturation loadings, we developed the isotherms shown in **Figures S.15**, **S.16**, and **S.17**.
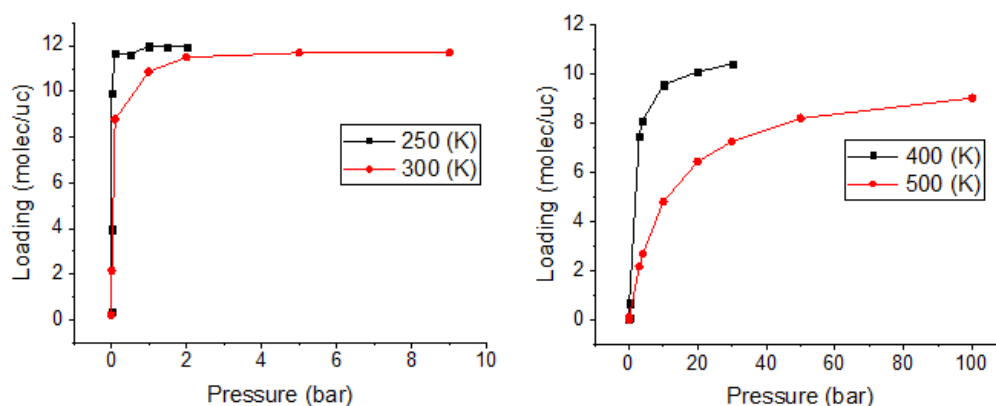
Figure S.15. Propane isotherms in bulk MFI.
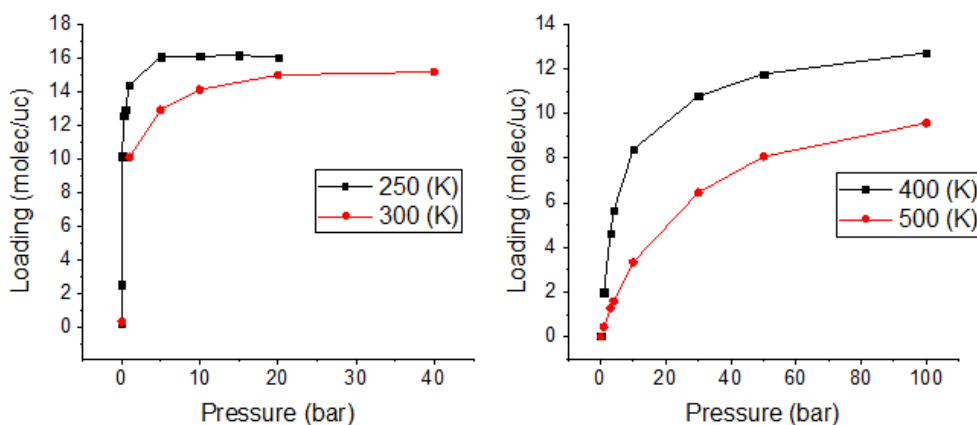
Figure S.16. Ethane isotherms in bulk MFI.
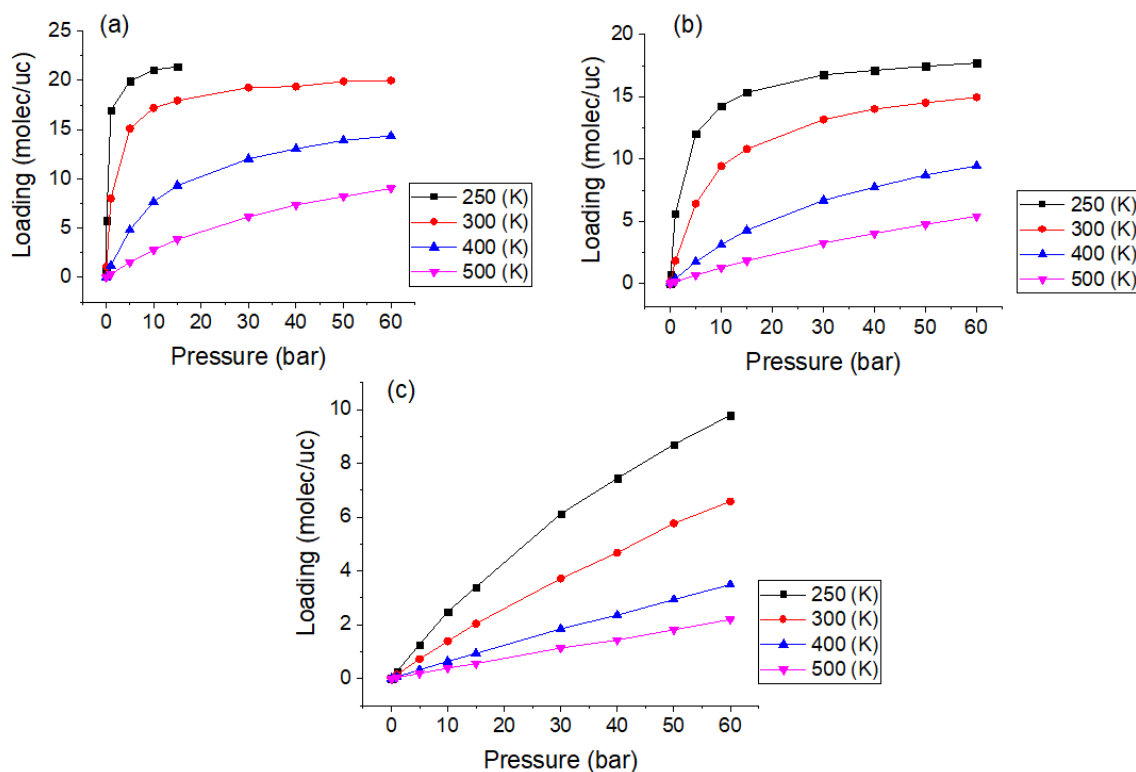
Figure S.17. (a) CO_2, (b) CH_4, and (c) H_2 isotherms in bulk MFI.

We determined the saturation pressure by visually observing were the curve became horizontal. The saturation pressures are shown in **Table S.9**. Though they were taken from the bulk isotherm, we used the same pressure to load both the bulk and slab unit cells. For species whose isotherm does not follow the standard shape, such as H_2, we simply chose a high pressure from within the examined pressure range. Additionally, the saturation pressure from the ethane isotherm was used for ethene and the saturation pressure from the propane isotherm was used for propene.

Table S.9 – Saturation Pressures

Temperature (K)	Pressure (bar)						
	H_2	CH_4	CO_2	ethane	ethene	propane	propene
250	60	30	15	1	1	0.5	0.5
300	60	30	30	20	20	3	3
400	60	30	30	30	30	30	30
500	60	30	30	30	30	30	30

S.10   All Ideal Selectivities

The ideal selectivities for H_2/CO_2, CH_4/CO_2, ethene/ethane, and propene/propane for MFI are shown in **Figure S.18**. For each case, the slab ideal selectivity is higher that the bulk ideal selectivity due to surface resistance having a larger effect on the molecule with the larger heat of adsorption.
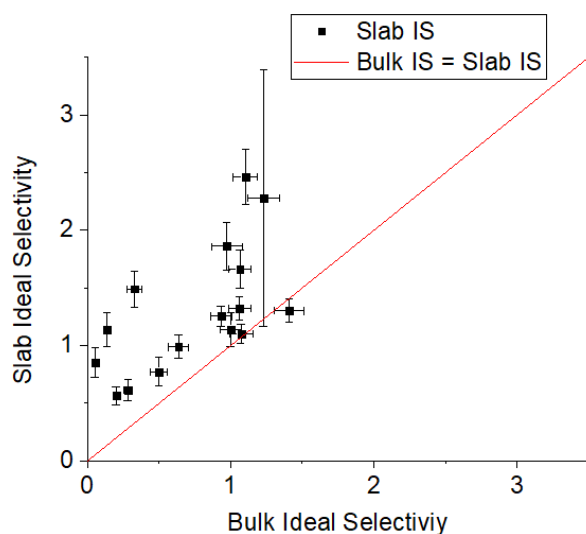
Figure S.18. The slab ideal selectivity and bulk ideal selectivity for H_2/CO_2, CH_4/CO_2, ethene/ethane, and propene/propane in bulk MFI and a 2 nm MFI (010) slab at 1 molec/uc and 250, 300, 400, and 500 K.

S.11 $D_{slab,LNR}$ Prediction for Six Frameworks
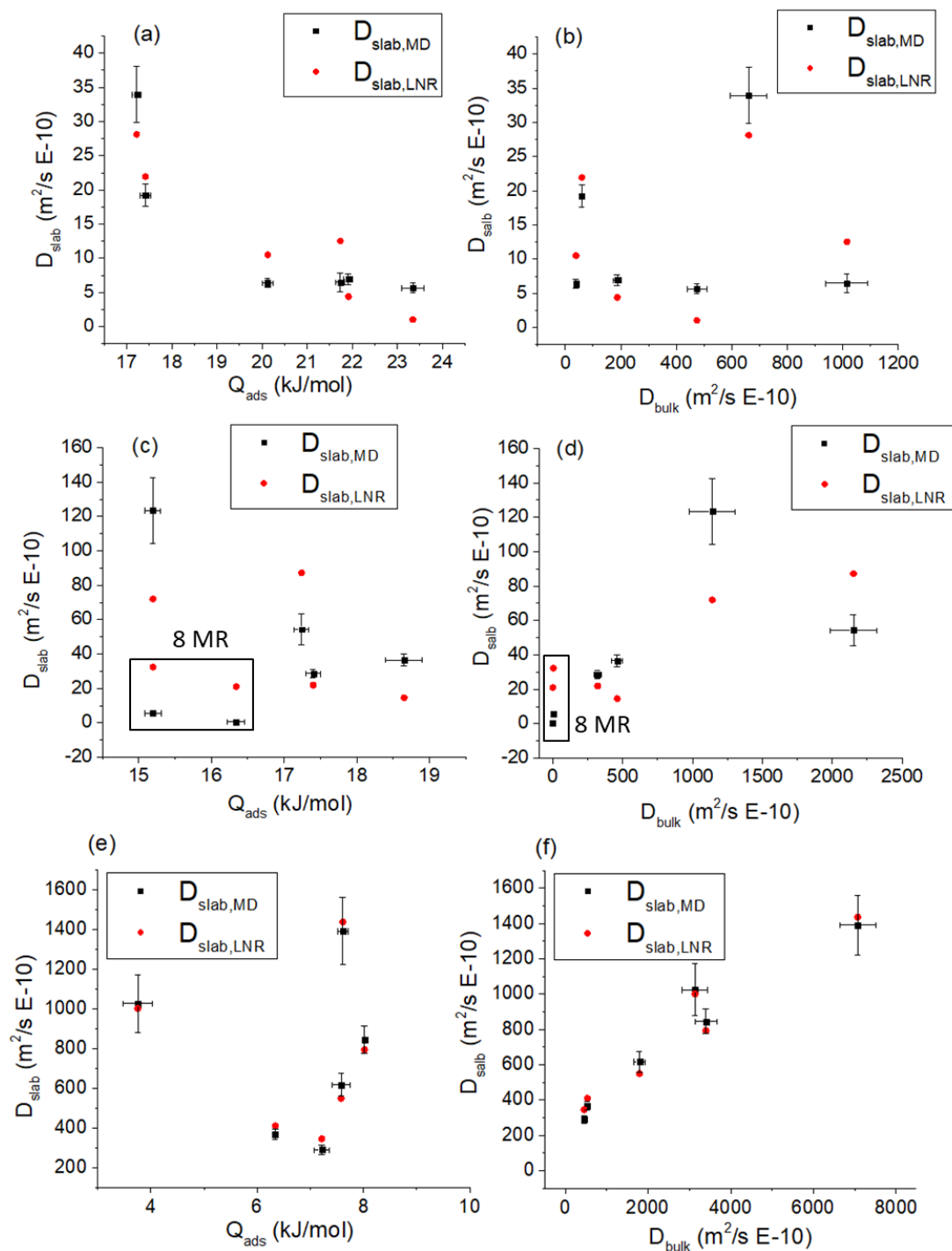
Figure S.19. The $D_{slab,MD}$ at 250 K and 1,689 Pa and the $D_{slab,LNR}$ graphed against Q_{ads} in (a) CO_2, (c) CH_4, and (e) H_2; graphed against D_{bulk} in (b) CO_2, (d) CH_4, and (f) H_2. The 8MR data is boxed in the CH_4 graphs in (c) and (d).

Table S.10 – Best Fit For D$_{slab}$ Estimate

	x_1 Unitless	x_2 (m²/s E-10)/(kJ/mol)	x_3 m²/s E-10	R^2 Fit
CO_2	0.001787	-0.83051	18.746	0.813
CH_4	0.034845	-9.7439	180.24	0.462
H_2	0.1685	-58.956	694.07	0.983

The IS$_{bulk}$ and IS$_{slab}$ results **in Figure S.20** show that for CO_2/CH_4, the IS$_{slab}$ increases with IS$_{bulk}$ while the opposite is true for CO_2/H_2. For CO_2/H_2 separation in the slab, surface resistance reduces CO_2 diffusion and gives a preference to H_2. For CO_2/CH_4 separation in the 10 MR zeolite slabs, there is no clear trend against the bulk diffusivity. This lack of trend is likely because CH_4 also has a surface resistance so it does not have quite the kinetic advantage in slab diffusion that H_2 has.
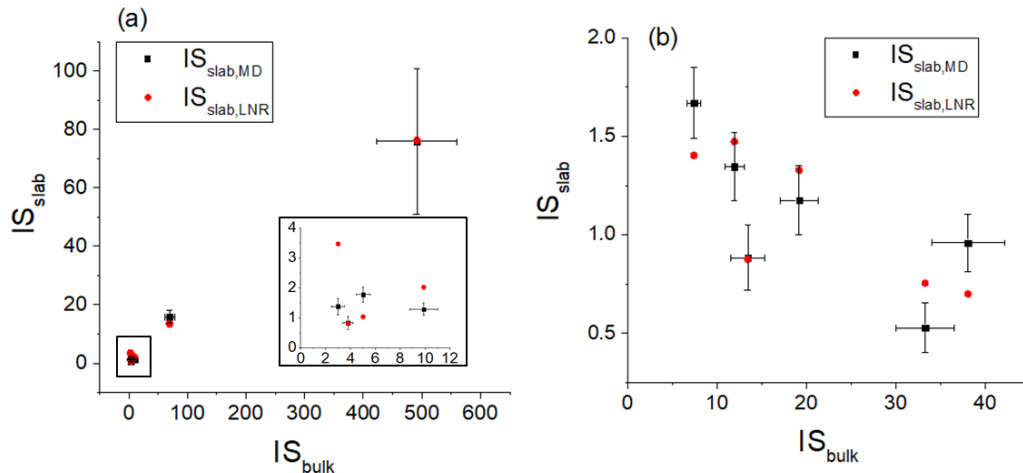
Figure S.20. Ideal selectivity of slab and bulk structures at 250 K and 1,689 Pa for (a) CO_2/CH_4 with an inset expanding the 10 MR zeolites, and (b) CO_2/H_2.

Table S.11 – Best Fit for IS$_{slab}$ Estimate

Slab Ideal Selectivity	x_1	x_2	x_3	R^2
	Unitless	1/(kJ/mol)	1/(kJ/mol)	
CO_2/CH_4	0.1532	-1.4462	1.8367	0.997
CO_2/H_2	-0.040186	0.059104	0.10573	0.707

S.12 Raw Data and Graph Data

Tables S**.12.1** to **S.12.8** display the raw diffusivity data from our calculations. They are not graphed in the main body of this manuscript but form the foundation for the graphs therein. The loading in nanosheets is the average number of adsorbates in the zeolite phase throughout the simulation. **Tables S.12.8** to **S.12.27** are the numerical data directly displayed in the main text graphs and are labeled as such.

Table S.12.1 – H$_2$ Diffusion at High and Low Loadings

	Bulk MFI (010)			2 nm MFI (010) Slab		
Temperature	Loading	$D_{z,zeo}$	S_m	Loading	$D_{z,zeo}$	S_m
K	molec/uc	m^2/s E-10	m^2/s E-10	molec/uc	m^2/s E-10	m^2/s E-10
250	2.00	1796	136	8.54	1022	80
300	2.00	2055	154	5.79	1283	100
400	2.00	1971	265	3.11	1999	211
500	2.00	3381	277	2.14	2216	206
250	20.00	1333	138	0.37	926	87
300	13.00	2131	186	0.30	1288	105
400	7.00	2691	251	0.22	1676	121
500	4.00	2800	316	0.18	2213	195

Table S.12.2 – CH$_4$ Diffusion at High and Low Loadings

	Bulk MFI (010)			2 nm MFI (010) Slab		
Temperature	Loading	$D_{z,zeo}$	S_m	Loading	$D_{z,zeo}$	S_m
K	molec/uc	m^2/s E-10	m^2/s E-10	molec/uc	m^2/s E-10	m^2/s E-10
250	2.00	321	25	0.95	28	2
300	2.00	349	27	0.86	55	6
400	2.00	552	42	0.69	156	22
500	2.00	647	52	0.55	276	21
250	33.00	292	22	22.21	115	10
300	26.00	317	23	15.36	137	11
400	13.00	559	39	7.44	226	20
500	6.00	720	57	4.24	273	47

Table S.12.3 – CO₂ Diffusion at High and Low Loadings

Temperature	Bulk MFI (010)			2 nm MFI (010) Slab		
K	Loading molec/uc	$D_{z,zeo}$ m²/s E-10	s_m m²/s E-10	Loading molec/uc	$D_{z,zeo}$ m²/s E-10	s_m m²/s E-10
250	2.00	188	15	0.99	7	1
300	2.00	225	18	0.96	20	2
400	2.00	339	29	0.84	80	6
500	2.00	434	32	0.69	155	10
250	44.00	85	7	39.75	38	3
300	38.00	160	13	27.67	61	7
400	24.00	286	22	12.80	111	8
500	12.00	421	29	6.87	147	15

Table S.12.4 – Ethene Diffusion at High and Low Loadings

Temperature	Bulk MFI (010)			2 nm MFI (010) Slab		
K	Loading molec/uc	$D_{z,zeo}$ m²/s E-10	s_m m²/s E-10	Loading molec/uc	$D_{z,zeo}$ m²/s E-10	s_m m²/s E-10
250	2	179	9	0.99	4	0
300	2	247	12	0.97	14	1
400	2	357	18	0.85	68	4
500	2	391	22	0.67	155	7
250	32	238	12	16.34	42	2
300	30	259	14	17.75	78	4
400	22	204	11	11.48	112	6
500	13	326	17	6.02	151	8

Table S.12.5 – Ethane Diffusion at High and Low Loadings

	Bulk MFI (010)			2 nm MFI (010) Slab		
Temperature	Loading	$D_{z,zeo}$	s_m	Loading	$D_{z,zeo}$	s_m
K	molec/uc	m²/s E-10	m²/s E-10	molec/uc	m²/s E-10	m²/s E-10
250	2	163	10	1.00	1	0
300	2	232	12	0.98	9	1
400	2	336	17	0.88	50	3
500	2	418	23	0.71	115	6
250	32	210	14	17.30	37	3
300	30	170	9	19.11	60	4
400	22	138	7	11.71	84	5
500	13	281	15	6.74	122	6

Table S.12.6 – Propene Diffusion at High and Low Loadings

	Bulk MFI (010)			2 nm MFI (010) Slab		
Temperature	Loading	$D_{z,zeo}$	s_m	Loading	$D_{z,zeo}$	s_m
K	molec/uc	m²/s E-10	m²/s E-10	molec/uc	m²/s E-10	m²/s E-10
250	2	106	6	1.00	0.3	0.1
300	2	159	8	0.99	3.0	0.3
400	2	132	27	0.94	26.6	3.4
500	2	259	28	0.78	69.3	7.8
250	24	3	0	10.79	8.0	0.4
300	23	26	3	11.13	21.2	2.7
400	21	62	8	13.41	44.9	4.5
500	15	161	17	7.51	95.0	9.6

Table S.12.7 – Propane Diffusion at High and Low Loadings

Temperature	Bulk MFI (010)			2 nm MFI (010) Slab		
	Loading	$D_{z,zeo}$	s_m	Loading	$D_{z,zeo}$	s_m
(K)	molec/uc	m^2/s E-10	m^2/s E-10	molec/uc	m^2/s E-10	m^2/s E-10
250	2	86	6	1.00	0.2	0.1
300	2	159	9	1.00	1.9	0.3
400	2	130	37	0.95	19.1	2.1
500	2	230	21	0.79	55.6	5.4
250	24	1	0	10.81	7.4	0.4
300	23	23	2	11.15	17.7	2.2
400	21	71	8	13.85	45.2	5.1
500	14	143	15	7.50	74.3	7.7

Table S.12.8 – Diffusion in a 14 nm MFI (010) Slab at 250 K and 1 molec/uc

Adsorbate	Loading molec/uc	$D_{z,zeo}$ m^2/s E-10	s_m m^2/s E-10
H_2	3.86	1470	72
CH_4	4.96	96	5
CO_2	4.99	41	2
Ethane	5.00	6	1
Propane	5.00	0.5	0.1

Table S.12.9 – Surface Resistance in 2 nm MFI at 1 molec/uc (Figure 2(a))

Temperature (K)	Surface Resistance (nm)						
	H_2	CH_4	CO_2	Ethene	Ethane	Propene	Propane
250	4.2	22.4	57.3	103.4	235.2	827.3	1537.1
300	3.3	12.6	20.9	34.5	56.3	114.4	183.7
400	4.7	6.3	7.3	9.6	12.9	8.2	12.1
500	4.3	2.9	4.1	3.5	5.7	6.3	7.1
	Surface Resistance Error (nm)						
250	0.8	2.8	8.4	7.7	23.6	286.7	551.1
300	0.6	2.0	3.0	3.0	5.1	14.2	29.4
400	1.1	1.4	1.1	0.9	1.1	2.5	4.4
500	0.8	0.6	0.6	0.4	0.6	1.3	1.2

Table S.12.10 – Surface Resistance in 2 nm MFI at High Loading (Figure 2(b))

Temperature (K)	Surface Resistance (nm)						
	H_2	CH_4	CO_2	Ethene	Ethane	Propene	Propane
250	0.7	3.4	2.7	10.2	10.3	-1.4	-1.8
300	1.4	2.9	3.5	5.1	4.0	0.5	0.7
400	0.8	3.2	3.4	1.8	1.4	0.9	1.2
500	0.6	3.6	4.1	2.6	2.8	1.5	2.0
	Surface Resistance Error (nm)						
250	0.4	0.6	0.6	0.9	1.3	0.1	0.1
300	0.4	0.6	0.8	0.5	0.5	0.4	0.5
400	0.4	0.6	0.6	0.3	0.3	0.5	0.5
500	0.4	1.1	0.8	0.4	0.4	0.5	0.6

Table S.12.11 – Surface Resistance vs. Heat of Adsorption (Figure 3)

| Temperature (K) | Surface Resistance (nm) | | | | | | |
	H_2	CH_4	CO_2	Ethene	Ethane	Propene	Propane
250	0.7	3.4	2.7	10.2	10.3	-1.4	-1.8
	Surface Resistance Error (nm)						
250	0.4	0.6	0.6	0.9	1.3	0.1	0.1
	Q_{ads} (kJ/mol)						
	7.6	16.3	21.8	23.2	26.0	31.2	33.7

Table S.12.12 – C$_2$ Ideal Selectivity in MFI (010) at 1 molec/uc (Figure 4(a))

| | Ethane/Ethene - Bulk | | Ethane/Ethene - Slab | |
Temperature (K)	IS	Error	IS	Error
250	1.1	0.1	2.7	0.6
300	1.1	0.1	1.6	0.2
400	1.0	0.1	1.3	0.1
500	0.9	0.1	1.2	0.1

Table S.12.13 – C$_2$ Ideal Selectivity in MFI (010) at High Loading (Figure 4(b))

| | Ethane/Ethene - Bulk | | Ethane/Ethene - Slab | |
Temperature (K)	IS	Error	IS	Error
250	1.1	0.1	0.9	0.1
300	1.5	0.1	1.2	0.1
400	1.4	0.1	1.3	0.1
500	1.1	0.1	1.1	0.1

Table S.12.14 – C$_3$ Ideal Selectivity in MFI (010) at 1 molec/uc (Figure 4(c))

| | Propane/Propene - Bulk | | Propene/Propane - Slab | |
Temperature (K)	IS	Error	IS	Error
250	1.2	0.1	2.3	1.1
300	1.0	0.1	1.6	0.3
400	1.0	0.4	1.4	0.2
500	1.1	0.2	1.2	0.2

Table S.12.15 – C$_3$ Ideal Selectivity in MFI (010) at High Loading (Figure 4(d))

Temperature (K)	Propane/Propene - Bulk		Propene/Propane - Slab	
	IS	Error	IS	Error
250	2.1	0.5	1.1	0.1
300	1.1	0.1	1.2	0.2
400	0.9	0.1	1.0	0.1
500	1.3	0.1	1.3	0.2

Table S.12.16 – H$_2$/CO$_2$ Ideal Selectivity in MFI (010) at 1 molec/uc (Figure 5(a))

Temperature (K)	H$_2$/CO$_2$ - Bulk		H$_2$/CO$_2$ - Slab	
	IS	Error	IS	Error
250	0.052	0.006	0.851	0.126
300	0.138	0.015	1.140	0.149
400	0.330	0.052	1.492	0.156
500	0.974	0.108	1.861	0.206

Table S.12.17 – CH$_4$/CO$_2$ Ideal Selectivity in MFI (010) at High Loading (Figure 5(b))

Temperature (K)	CH$_4$/CO$_2$ - Bulk		CH$_4$/CO$_2$ - Slab	
	IS	Error	IS	Error
250	2.1	0.5	1.1	0.1
300	1.1	0.1	1.2	0.2
400	0.9	0.1	1.0	0.1
500	1.3	0.1	1.3	0.2

Table S.12.18 – Surface Resistance at 2 bar 300 K (Figure 6(a))

Slab Height (nm)	Surface Resistance (nm)		
	H_2	CH_4	CO_2
1	1.1	5.0	6.9
2	1.9	9.1	12.1
4	1.3	8.9	16.8
10	1.2	8.2	16.1
14	1.6	10.6	17.3
	Surface Resistance Error (nm)		
1	0.2	0.7	0.6
2	0.4	2.0	1.3
4	0.4	1.6	1.4
10	0.8	2.3	1.8
14	1.1	2.9	2.1

Table S.12.19 – Surface Resistance at 2 bar 400 K (Figure 6(b))

Slab Height (nm)	Surface Resistance (nm)		
	H_2	CH_4	CO_2
1	0.6	3.6	3.7
2	0.3	3.6	6.0
4	0.7	4.3	6.3
10	0.0	6.0	6.8
14	1.6	3.1	6.3
	Surface Resistance Error (nm)		
1	0.2	0.4	0.4
2	0.3	0.6	0.8
4	0.3	0.8	0.9
10	0.7	1.5	1.5
14	1.1	1.5	1.8

Table S.12.20 – Surface Resistance at 20 bar 300 K (Figure 6(c))

Slab Height (nm)	Surface Resistance (nm)		
	H_2	CH_4	CO_2
1	0.9	3.7	3.6
2	1.7	4.1	4.4
4	1.8	5.0	2.8
10	1.3	4.9	3.7
14	0.3	2.3	2.7
	Surface Resistance Error (nm)		
1	0.2	0.4	0.3
2	0.5	0.6	0.5
4	0.5	0.8	0.5
10	0.9	1.4	0.9
14	1.1	1.5	1.1

Table S.12.21 – Surface Resistance at 20 bar 400 K (Figure 6(d))

Slab Height (nm)	Surface Resistance (nm)		
	H_2	CH_4	CO_2
1	1.1	3.5	3.2
2	1.5	4.0	3.9
4	1.6	4.3	3.3
10	2.6	4.8	3.8
14	2.7	4.6	4.6
	Surface Resistance Error (nm)		
1	0.2	0.4	0.4
2	0.3	0.6	0.5
4	0.5	0.8	0.6
10	1.1	1.4	1.1
14	1.3	1.7	1.6

Table S.12.22 – Surface Resistance vs. Height in MFI Slabs (Figure 7 of Main Text)

Slab Height (nm)	Surface Resistance (nm)				
	H_2	CH_4	CO_2	Ethane	Propane
2	2	23	58	265	1181
10	2	24	37	256	1780
	Surface Resistance Error (nm)				
2	1	3	8	56	554
10	1	3	5	65	549

Table S.12.23 – Surface Resistance in Different Frameworks (Figure 8(a))

Framework	Surface Resistance (nm)		
	H_2	CH_4	CO_2
LTA	1.1	-0.3	5.4
CHA	1.1	0.4	10.1
AFI	4.6	18.6	41.5
MFI	4.2	22.4	57.3
AEL	6.9	26.4	189.4
ATO	11.1	105.3	425.8
	Surface Resistance Error (nm)		
LTA	0.4	0.3	0.9
CHA	0.3	0.8	1.5
AFI	1.2	4.4	6.8
MFI	0.8	2.8	8.4
AEL	1.0	3.7	28.5
ATO	1.9	19.9	94.3

Table S.12.24 – CO$_2$ D$_{0,bulk}$, D$_{0,slab}$, and Q$_{ads}$ in Different Frameworks (Figures 8(b) and S.19)

Framework	D$_{0,bulk}$ m^2/s E-10	D$_{0,slab,MD}$ m^2/s E-10	Q$_{ads}$ kJ/mol	D$_{0,slab,LNR}$ m^2/s E-10
MFI	188	7	21.9	4
AEL	474	6	23.3	1
ATO	1015	6	21.7	13
AFI	661	34	17.2	28
LTA	60	19	17.4	22
CHA	39	6	20.1	10
		Errors		
MFI	15	1	0.1	
AEL	36	1	0.3	
ATO	76	1	0.1	
AFI	65	4	0.1	
LTA	4	2	0.1	
CHA	2	1	0.1	

Table S.12.25 – CH$_4$ D$_{0,bulk}$, D$_{0,slab}$, and Q$_{ads}$ in Different Frameworks (Figures 8(c) and S.19)

Framework	D$_{0,bulk}$ m^2/s E-10	D$_{0,slab,MD}$ m^2/s E-10	Q$_{ads}$ kJ/mol	D$_{0,slab,LNR}$ m^2/s E-10
MFI	321	29	17.4	22
AEL	462	37	18.7	15
ATO	2152	54	17.2	87
AFI	1142	123	15.2	72
LTA	5	6	15.2	32
CHA	1	1	16.3	21
		Errors		
MFI	25	2	0.6	
AEL	40	4	0.4	
ATO	167	9	0.3	
AFI	163	19	0.4	
LTA	0.5	0.6	0.3	
CHA	0.1	0.2	0.5	

Table S.12.26 – H_2 $D_{0,bulk}$, $D_{0,slab}$, and Q_{ads} in Different Frameworks (Figures 3.8(d) and S.19)

Framework	$D_{0,bulk}$ m^2/s E-10	$D_{0,slab,MD}$ m^2/s E-10	Q_{ads} kJ/mol	$D_{0,slab,LNR}$ m^2/s E-10
MFI	1796	617	7.6	550
AEL	3397	845	8.0	794
ATO	7068	1390	7.6	1436
AFI	3134	1025	3.8	1001
LTA	534	368	6.3	410
CHA	453	290	7.2	345
Errors				
MFI	136	58	0.6	
AEL	260	70	0.4	
ATO	436	170	0.3	
AFI	306	146	0.4	
LTA	38	25	0.3	
CHA	31	23	0.5	

Table S.12.27 – Slab Ideal Selectivity (Figure 9 of Main Text)

Framework	MD CO_2/CH_4	LNR CO_2/CH_4	MD CO_2/H_2	LNR CO_2/H_2
MFI	1.8	1.0	1.2	1.3
AEL	1.3	2.0	1.0	0.7
ATO	0.8	0.8	0.5	0.8
AFI	1.4	3.5	0.9	0.9
LTA	15.9	13.4	1.7	1.4
CHA	75.9	76.2	1.3	1.5
Errors				
MFI	0.3		0.2	
AEL	0.2		0.1	
ATO	0.2		0.1	
AFI	0.3		0.2	
LTA	2.1		0.2	
CHA	25.0		0.2	

S.13   Software

-Vienna Ab Initio Simulation Package (VASP 5.4.4):[39] used for generating DFT energies for CO_2 and H_2 force field fitting.

-Large-scale Atomic/Molecular Massively Parallel Simulator (LAMMPS) version 08/22/2018:[40, 41] used for all equilibrium molecular dynamics simulations.

-RASPA 2014 (Version 2.0):[42] used for GCMC simulations to generate isotherms and load unit cells.

-Pymatgen 4.4.0[43] and Atomic Simulation Environment (ASE) 3.11.10:[44] used to read unit cells into our python file that generated the Hill Sauer data file.

-2D nanosheet database:[45] nanosheets used in the study were downloaded from the Knio et al. database.

-Matlab R2016b (9.1.0.441655), September 7, 2016:[46] the fitlm() function was used to predict diffusivities and ideal selectivities for slabs of six different frameworks.

S.14   Supporting Information References

(1) Boulfelfel, S. E.; Ravikovitch, P. I.; Koziol, L.; Sholl, D. S. Improved Hill–Sauer force field for accurate description of pores in 8-ring zeolites. *J. Phys. Chem. C.* **2016**, 120(26), 14140-14148.

(2) Plimpton, S.; Crozier, P.; Thompson, A. LAMMPS-large-scale atomic/molecular massively parallel simulator. *Sandia National Laboratories* **2007**, 18.

(3) Hill, J.-R.; Sauer, J. Molecular mechanics potential for silica and zeolite catalysts based on ab initio calculations. 2. Aluminosilicates. *J. Phys. Chem.* **1995**, 99(23), 9536-9550.

(4) Boulfelfel, S. E.; Ravikovitch, P. I.; Sholl, D. S. Modeling diffusion of linear hydrocarbons in silica zeolite LTA using transition path sampling. *J. Phys. Chem. C.* **2015**, 119(27), 15643-15653.

(5) Fang, H.; Kamakoti, P.; Zang, J.; Cundy, S.; Paur, C.; Ravikovitch, P. I.; Sholl, D. S. Prediction of CO_2 Adsorption Properties in Zeolites Using Force Fields Derived from Periodic Dispersion-Corrected DFT Calculations. *J. Phys. Chem. C.* **2012**, 116(19), 10692-10701.

(6) Fang, H. J.; Awati, R.; Boulfelfel, S. E.; Ravikovitch, P. I.; Sholl, D. S. First-Principles-Derived Force Fields for CH_4 Adsorption and Diffusion in Siliceous Zeolites. *J. Phys. Chem. C.* **2018**, 122(24), 12880-12891.

(7) Manz, T. A.; Sholl, D. S. Chemically Meaningful Atomic Charges That Reproduce the Electrostatic Potential in Periodic and Nonperiodic Materials. *J. Chem. Theory Comput.* **2010**, 6(8), 2455-2468.

(8) Watanabe, T.; Manz, T. A.; Sholl, D. S. Accurate Treatment of Electrostatics during Molecular Adsorption in Nanoporous Crystals without Assigning Point Charges to Framework Atoms. *J. Phys. Chem. C.* **2011**, 115(11), 4824-4836.

(9) Manz, T. A.; Sholl, D. S. Methods for Computing Accurate Atomic Spin Moments for Collinear and Noncollinear Magnetism in Periodic and Nonperiodic Materials. *J. Chem. Theory Comput.* **2011**, 7(12), 4146-4164.

(10) Harris, J. G.; Yung, K. H. Carbon dioxide's liquid-vapor coexistence curve and critical properties as predicted by a simple molecular model. *J. Phys. Chem.* **1995**, 99(31), 12021-12024.

(11) Boulfelfel, S. E.; Ravikovitch, P. I.; Koziol, L.; Sholl, D. S. Improved Hill-Sauer Force Field for Accurate Description of Pores in 8-Ring Zeolites. *J. Phys. Chem. C.* **2016**, 120(26), 14140-14148.

(12) Hill, J. R.; Sauer, J. Molecular Mechanics Potential for Silica and Zeolite Catalysts Based on Ab-Initio Calculations .2. Aluminosilicates. *J. Phys. Chem.* **1995**, 99(23), 9536-9550.

(13) Yang, Q. Y.; Xu, Q.; Liu, B.; Zhong, C. L.; Smit, B. Molecular Simulation of CO_2/H_2 Mixture Separation in Metal-organic Frameworks: Effect of Catenation and Electrostatic Interactions. *Chin. J. Chem. Eng.* **2009**, 17(5), 781-790.

(14) Fiorin, G.; Klein, M. L.; Henin, J. Using collective variables to drive molecular dynamics simulations. *Mol. Phys.* **2013**, 111(22-23), 3345-3362.

(15) Plimpton, S. Fast Parallel Algorithms for Short-Range Molecular-Dynamics. *J. Comput. Phys.* **1995**, 117(1), 1-19.

(16) Grimme, S. Semiempirical GGA-type density functional constructed with a long-range dispersion correction. *J. Comput. Chem.* **2006**, 27(15), 1787-1799.

(17) Kresse, G.; Hafner, J. Abinitio Molecular-Dynamics for Liquid-Metals. *Phys. Rev. B.* **1993**, 47(1), 558-561.

(18) Kresse, G.; Hafner, J. Ab-Initio Molecular-Dynamics Simulation of the Liquid-Metal Amorphous-Semiconductor Transition in Germanium. *Phys. Rev. B.* **1994**, 49(20), 14251-14269.

(19) Kresse, G.; Furthmuller, J. Efficiency of ab-initio total energy calculations for metals and semiconductors using a plane-wave basis set. *Comp. Mater. Sci.* **1996**, 6(1), 15-50.

(20) Kresse, G.; Furthmuller, J. Efficient iterative schemes for ab initio total-energy calculations using a plane-wave basis set. *Phys. Rev. B.* **1996**, 54(16), 11169-11186.

(21) Blochl, P. E. Projector Augmented-Wave Method. *Phys. Rev. B.* **1994**, 50(24), 17953-17979.

(22) Kresse, G.; Joubert, D. From ultrasoft pseudopotentials to the projector augmented-wave method. *Phys. Rev. B.* **1999**, 59(3), 1758-1775.

(23) Fang, H. J.; Kamakoti, P.; Ravikovitch, P. I.; Aronson, M.; Paur, C.; Sholl, D. S. First principles derived, transferable force fields for CO_2 adsorption in Na-exchanged cationic zeolites. *Phys. Chem. Chem. Phys.* **2013**, 15(31), 12882-12894.

(24) Pulido, A.; Delgado, M. R.; Bludsky, O.; Rubes, M.; Nachtigall, P.; Arean, C. O. Combined DFT/CC and IR spectroscopic studies on carbon dioxide adsorption on the zeolite H-FER. *Energy Environ. Sci.* **2009**, 2(11), 1187-1195.

(25) Arean, C. O.; Palomino, G. T.; Carayol, M. R. L.; Pulido, A.; Rubes, M.; Bludsky, O.; Nachtigall, P. Hydrogen adsorption on the zeolite Ca-A: DFT and FT-IR investigation. *Chem. Phys. Lett.* **2009**, 477(1-3), 139-143.

(26) Darkrim, F.; Levesque, D. Monte Carlo simulations of hydrogen adsorption in single-walled carbon nanotubes. *J. Chem. Phys.* **1998**, 109(12), 4981-4984.

(27) Pham, T. D.; Lobo, R. F. Adsorption equilibria of CO_2 and small hydrocarbons in AEI-, CHA-, SIT-, and RRO-type siliceous zeolites. *Microporous Mesoporous Mater.* **2016**, 236, 100-108.

(28) Bai, P.; Tsapatsis, M.; Siepmann, J. I. TraPPE-zeo: Transferable potentials for phase equilibria force field for all-silica zeolites. *J. Phys. Chem. C.* **2013**, 117(46), 24375-24387.

(29) Martin, M. G.; Siepmann, J. I. Transferable potentials for phase equilibria. 1. United-atom description of n-alkanes. *J. Phys. Chem. B.* **1998**, 102(14), 2569-2577.

(30) Wick, C. D.; Martin, M. G.; Siepmann, J. I. Transferable potentials for phase equilibria. 4. United-atom description of linear and branched alkenes and alkylbenzenes. *J. Phys. Chem. B.* **2000**, 104(33), 8008-8016.

(31) Hill, J. R.; Sauer, J. Molecular mechanics potential for silica and zeolite catalysts based on ab initio calculations. 1. Dense and microporous silica. *J. Phys. Chem.* **1994**, 98(4), 1238-1244.

(32) Granato, M. A.; Vlugt, T. J.; Rodrigues, A. E. Molecular simulation of propane− propylene binary adsorption equilibrium in zeolite 13X. *Ind. Eng. Chem. Res.* **2007**, 46(22), 7239-7245.

(33) Fang, H.; Awati, R.; Boulfelfel, S. E.; Ravikovitch, P. I.; Sholl, D. S. First-principles-derived force fields for CH_4 adsorption and diffusion in siliceous zeolites. *J. Phys. Chem. C.* **2018**, 122(24), 12880-12891.

(34) Newsome, D. A.; Sholl, D. S. Predictive assessment of surface resistances in zeolite membranes using atomically detailed models. *J. Phys. Chem. B.* **2005**, 109(15), 7237-7244.

(35) Liu, L.; Nicholson, D.; Bhatia, S. K. Interfacial resistance and length-dependent transport diffusivities in carbon nanotubes. *J. Phys. Chem. C.* **2016**, 120(46), 26363-26373.

(36) Sellers, H.; Gislason, J. Adsorption and desorption rate constants for small molecules on metal surfaces: an example of Trouton's rule. *Surf. Sci.* **1999**, 426(2), 147-153.

(37) Pranami, G.; Lamm, M. H. Estimating error in diffusion coefficients derived from molecular dynamics simulations. *J. Chem. Theory Comput.* **2015**, 11(10), 4586-4592.

(38) Dutta, R. C.; Bhatia, S. K. Interfacial barriers to gas transport in zeolites: distinguishing internal and external resistances. *Phys. Chem. Chem. Phys.* **2018**, 20(41), 26386-26395.

(39) Hafner, J.; Kresse, G., The vienna ab-initio simulation program vasp: An efficient and versatile tool for studying the structural, dynamic, and electronic properties of materials. In *Properties of Complex Inorganic Solids*, Springer: 1997; pp 69-82.

(40) Brown, W. M.; Wang, P.; Plimpton, S. J.; Tharrington, A. N. Implementing molecular dynamics on hybrid high performance computers–short range forces. *Comput. Phys. Commun.* **2011**, 182(4), 898-911.

(41) Kresse, G.; Furthmüller, J. Efficient iterative schemes for ab initio total-energy calculations using a plane-wave basis set. *Phys. Rev. B.* **1996**, 54(16), 11169.

(42) Dubbeldam, D.; Calero, S.; Ellis, D. E.; Snurr, R. Q. RASPA: molecular simulation software for adsorption and diffusion in flexible nanoporous materials. *Mol. Simul.* **2016**, 42(2), 81-101.

(43) Tran, R.; Xu, Z.; Radhakrishnan, B.; Winston, D.; Sun, W.; Persson, K. A.; Ong, S. P. Surface energies of elemental crystals. *Sci. Data.* **2016**, 3, 160080.

(44) Larsen, A. H.; Mortensen, J. J.; Blomqvist, J.; Castelli, I. E.; Christensen, R.; Dułak, M.; Friis, J.; Groves, M. N.; Hammer, B.; Hargus, C. The atomic simulation environment—a Python library for working with atoms. *J. Phys.: Condens. Matter.* **2017**, 29(27), 273002.

(45) Knio, O.; Medford, A. J.; Nair, S.; Sholl, D. S. Database of Computation-Ready 2D Zeolitic Slabs. *Chem. Mater.* **2018**, 31(2), 353-364.

(46) *MATLAB*, R2016b (9.1.0.441655); The MathWorks Inc.: Natick, Massachusetts.